MNRAS 000, 1–9 (2020) Preprint April 2, 2024 Compiled using MNRAS LATEX style file v3.0

# Lyman-alpha opacities at z=4-6 require low mass, radiatively-suppressed galaxies to drive cosmic reionization.

Pierre Ocvirk[1], Joseph S. W. Lewis[1], Nicolas Gillet[1], Jonathan Chardin[1], Dominique Aubert[1], Nicolas Deparis[1] & Émilie Thélie[1]
[1]*Observatoire Astronomique de Strasbourg, Université de Strasbourg, CNRS UMR 7550, 11 rue de l'Université, 67000 Strasbourg, France*



Accepted XXX. Received YYY; in original form ZZZ

**ABSTRACT**

The high redshift Lyman-$\alpha$ forest, in particular the Gunn-Peterson trough, is the most unambiguous signature of the neutral to ionized transition of the intergalactic medium (IGM) taking place during the Epoch of Reionization (EoR). Recent studies, e.g. Kulkarni et al. (2019a); Keating et al. (2019), showed that reproducing the observed Lyman-$\alpha$ opacities after overlap required a non-monotonous evolution of cosmic emissivity: rising, peaking at z$\sim$ 6, and then decreasing onwards to z=4. Such an evolution is puzzling considering galaxy buildup and the cosmic star formation rate are still continously on the rise at these epochs. Here, we use new RAMSES-CUDATON simulations to show that such a peaked evolution may occur naturally in a fully coupled radiation-hydrodynamical framework, due to radiative suppression of star formation. In our best matching run, cosmic emissivity at z>6 is dominated by a low mass ($M_{DM} < 2.10^9 M_\odot$), high escape fraction halo population, driving reionization, up to overlap. Approaching z=6, this population is radiatively suppressed due to the rising ionizing UV background, and its emissivity drops. In the meantime, the high mass, low escape fraction, halo population builds up and its emissivity rises, but not fast enough to compensate the dimming of the low mass haloes. The combined ionizing emissivity of these two populations therefore naturally results in a rise and fall of the cosmic emissivity, from z=12 to z=4, with a peak at z$\sim$ 6. An alternative simulation, which features a later suppression and higher escape fractions for the high mass haloes, leads to overshooting the ionizing rate, over-ionizing the IGM and therefore too low Lyman-$\alpha$ opacities.

**Key words:** reionisation - galaxies: formation - high redshift - Lyman alpha forest

## 1 INTRODUCTION

The epoch of reionization (hereafter EoR) starts when the first stars begin producing neutral hydrogen (HI) ionizing photons, resulting in growing ionized regions in the intergalactic medium (hereafter IGM). In its simplest form, the EoR begins with the formation of the first pristine, metal-free stars stars at redshifts as high as z=30, with star formation taking place to progressively larger metal-rich haloes. However, modelling this process is made complicated by the fact that describing the progress and sources of reionization involves a number of (poorly constrained) parameters, such as the minimum halo mass of star-forming galaxies and their star-formation efficiency. Despite recent advances in observations and theory, the debate is still ongoing with respect to the nature of the sources powering reionization. Several studies have ruled out high-redshift active galactic nuclei as a main player, predicting them to contribute only a few percent to cosmic reionization (Mitra et al. 2018; Matsuoka et al. 2018; Kulkarni et al. 2019b). Then, focusing on galaxies, several recent, full radiation-hydrodynamical (hereafter RHD) studies have predicted that galaxies should be able to reionize the Universe on their own, provided their stellar populations provide enough ionizing photons ((Rosdahl et al. 2018; Ocvirk et al. 2018). However, the jury is still out concerning what class of galaxies are the main drivers of cosmic reionization. Most studies favor low mass or intermediate mass systems (Wise 2019; Katz et al. 2019; Lewis et al. 2020), contrasting with other studies favoring high mass galaxies as the most proficient reionizers (Naidu et al. 2020). Even more uncertain are the properties of these galaxies: what is their ionizing escape fraction, how do they react to supernova feedback and irradiation from internal and external sources?

These recent theoretical studies, despite methodological differences, reproduce fairly well a number of high-redshift observables related to the EoR, in particular the UV galaxy luminosity function, the electron-scattering optical depth seen by the cosmic microwave background, and the timing of reionization, completing reionization between z=5.3-6 , such as in Kulkarni et al. (2019a) (hereinafter K19). However, beyond the *timing* of reionization, one particular constraint that RHD EoR studies have left relatively untapped is the post-overlap average neutral fraction, i.e. the residual neutral

fraction remaining once reionization is finished, as determined for instance by Fan et al. (2006) (hereinafter F06), and we offer below some elements of thought as to why this constraint has perhaps not received the attention it should in full RHD simulations.

First of all, it appears the post-overlap residual neutral fraction $x_{HI}^{res}$ is surprisingly difficult to reproduce in RHD simulations, as well as in naive post-processing regimes, and it is common to see deviations from Fan et al. (2006) values in the literature, even when the timing of reionization is well reproduced (Aubert & Teyssier 2010; Petkova & Springel 2011; Zawada et al. 2014; So et al. 2014; Bauer et al. 2015; Aubert et al. 2015; Ocvirk et al. 2016; Aubert et al. 2018; Ocvirk et al. 2019; Wu et al. 2019a; Ocvirk et al. 2018). In Ocvirk et al. (2018), for instance, the residual neutral fraction is too low because the ionizing rate is too high, and the Universe ends up too transparent. Some works seem to fare better than others in this respect Rosdahl et al. (2018); Katz et al. (2018), but the interpretation of the apparent better match obtained is complicated by the use of a reduced or variable speed of light formalism, which has been shown to strongly impact the residual neutral fraction $x_{HI}^{res}$ (Gnedin 2016; Ocvirk et al. 2019; Wu et al. 2019a,b), as well as its timing (Bauer et al. 2015; Deparis et al. 2019). This now long-lasting difficulty in reproducing accurately the Fan et al. (2006) residual hydrogen neutral fractions in RHD simulations has led a number of authors to simply not show the evolution of the neutral hydrogen fraction in their papers any more, and instead show the evolution of the *ionized* fraction with redshift, or resort to using a linear scale, which easily hides any discrepancy on the residual *neutral* fraction. Let us recognize, though, that this reserve in comparing simulation results with the neutral hydrogen fraction from e.g. F06 is partly well-founded: indeed, the neutral fraction $xHI_{res}$ is not a direct observable, but the result of the modeling of the opacities of the high-z Lyman-alpha forest. Therefore, the $xHI_{res}$ of F06 depends on assumptions regarding cosmology, the gas density distribution, and the radiation field the gas is exposed to. It is therefore preferable to work directly with these opacities than with the residual neutral hydrogen fraction when comparing simulations and observations, and this requires computing pseudo-spectra of hydrogen transmission along lines-of-sight through the simulated volume. In this direction, K19 and Keating et al. (2019) have shown that the statistical properties of the high-z Lyman-alpha forest could be well reproduced if reionization finished by redshift z$\sim$ 5.3, i.e. significantly later than the commonly assumed value of z=6, but it also required a fine-tuned, non-monotonous comoving ionizing emissivity, with a marked *decrease* after z=6, in stark contrast with, e.g., the evolution of comoving star formation density, which is always monotonously increasing at the relevant epochs, because dark matter haloes keep building up, as shown in Ocvirk et al. (2016, 2018) and Bouwens et al. (2015). This fine-tuning is found in different forms in a number of other works, e.g. Chardin et al. (2015, 2017); Chardin et al. (2018). While allowing for exquisite fidelity in reproducing high-z spectra of the Lyman-alpha forest, this framework leaves the question of how this fine-tuning of the emissivity arises an open matter. In full RHD simulations, such a fine-tuning of the co-moving ionizing emissivity is not possible, because it is intrinsically, self-consistently tied to the star formation of galactic haloes and their ionizing escape fractions, which are both an outcome of the simulation, and can not be tuned or modulated as the simulation runs. Without this fine-tuning, it is very difficult to reproduce correctly the post-overlap Lyman-alpha forest at z=4-6, even just in average opacity. A similar conclusion was reached by Madau (2017): "... simple models where the product of the two unknowns [ionizing escape fraction and stellar ionizing emissivity] is not evolving with redshift fail to reproduce the changing neutrality of the IGM observed at these epochs." Acknowledging this, some works take the route of using an evolving escape fraction Dayal et al. (2020), which results in a peak or plateau of stellar emissivity, and then a decrease. However, it may be desirable, as we do in this work, to go beyond a simple global escape fraction framework, because most numerical works point at the escape fraction being first and foremost a strong function of halo mass. Other studies, for instance, achieve good post-overlap neutral fraction by invoking dust formation, conveniently turning down galaxy escape fraction between z=8 and 6 Gnedin & Kaurov (2014); Puchwein et al. (2019). Such a dust-related decrease in galaxy escape fraction may indeed happen, as shown in some simulations (Yoo et al. 2020). However, is dust the only possible process allowing for a drop in cosmic emissivity? Also, is there actually enough dust at high redshift and in the right places to account for this drop? We leave these considerations for another time, as it is sure to be a hotly debated topic for a while. For now, it stands that a rising, then decreasing ionizing emissivity around overlap, as in K19, is required to obtain reasonable opacities in the high-z, post-overlap Lyman-alpha forest. Without dust, this is puzzling because the build-up of the galaxy population is ongoing at these epochs, and the cosmic star formation rate keeps on rising monotonically. If we take this requirement at face value, what could be the physical process(es) promoting the decrease of the ionizing emissivity? Can it be reproduced self-consistently in a fully coupled RHD simulation? These are the questions we set up to address in this paper. We will present a set of fully-coupled RHD simulations, displaying a strong radiative feedback which reduces star formation in low mass haloes. In the best-matching simulation, these low mass haloes are also the main drivers of cosmic reionization. Therefore, as their star formation is suppressed by progressing reionization, the average ionizing emissivity goes down. This suggests that external radiative suppression of star formation in low mass haloes is a crucial mechanism in reproducing the transmission properties of the Lyman-alpha forest during the EoR and after overlap. The paper plan is as follows. Section 2 details the simulations performed, Sec. 3, their analysis and our results, before concluding in Sec. 4.

## 2 SIMULATIONS

We use the numerical simulation code RAMSES-CUDATON, as presented in Ocvirk et al. (2016, 2018). The code couples RAMSES Teyssier (2002) with the radiative transfer module ATON Aubert & Teyssier (2008), resulting in a fully coupled radiation-hydrodynamics code for galaxy formation in a cosmological context. The radiative transfer module is optimized for running on Graphics Processing Units (GPUs), as described in Aubert & Teyssier (2010), taking advantage of their massive parallel computing power, hence the CUDA keyword. RAMSES handles the cosmological context, gravity, hydrodynamics, star formation and supernova feedback, including chemical enrichment, while ATON/CUDATON computes ionizing photon propagation and interaction with the hydrogen gas (photo-ionization, photo-heating and cooling processes). The code has been deployed on a variety of supercomputers, and has allowed us to produce the largest ever simulations of the EoR, Cosmic Dawn I and II (CoDa I and II), presented in Ocvirk et al. (2016, 2018). As an evolution beyond CoDa II, which was well calibrated with respect to a number of observables of the EoR, the setup for our new simulations is similar in many ways, but differs in some key aspects. First of all, we are using here a 2 times higher spatial resolution, and 8 times higher mass resolution, in order to better resolve the range

| Cosmology (Planck14) | |
|---|---|
| Dark energy density $\Omega_\Lambda$ | 0.693 |
| Matter density $\Omega_m$ | 0.307 |
| Baryonic matter density $\Omega_b$ | 0.048 |
| Hubble constant $h = H_0/(100\,km/s)$ | 0.677 |
| Power spectrum | |
| Normalization $\sigma_8$ | 0.8288 |
| Index $n$ | 0.963 |
| **Setup** | |
| Grid size | $1024^3$ |
| Comoving box size | 11.8 Mpc (8 $h^{-1}$Mpc ) |
| Comoving force resolution dx | 11.53 kpc |
| Physical force resolution at z=6 | 1.65 kpc |
| DM particle number $N_{DM}$ | $1024^3$ |
| DM particle mass $M_{DM}$ | 5.09 x $10^4$ $M_\odot$ |
| Average cell gas mass | 9.375 x $10^3$ $M_\odot$ |
| Initial redshift $z_{start}$ | 150 |
| End redshift $z_{end}$ | 4.0 |
| **Star formation** | |
| Density threshold $\delta_\star$ | 50 $\langle\rho_{gas}\rangle$ |
| Temperature threshold $T_\star$ | |
| Strict | $2 \times 10^4$K |
| Permissive | none |
| Efficiency $\epsilon_\star$ | |
| Strict | 0.03 |
| Permissive | 0.02 |
| **[♣ CHECK STELLAR MASS]** | |
| Stellar particle birth mass $M_\star$ | 11732 $M_\odot$ |
| **Feedback** | |
| Massive star lifetime $t_\star$ | 10 Myr |
| **Supernova** | |
| Mass fraction $\eta_{SN}$ | 20% |
| Energy $E_{SN}$ | $10^{51}$ erg |
| Metal yield $y$ | 10% |
| **Radiation** | |
| Stellar population model | BPASSv2.2.1 |
| Stellar particle escape fraction $f_{esc}^{sub}$ | |
| Strict | 1 |
| Permissive | 0.45 |
| Effective photon energy $\bar{\epsilon}$ | 21.74 eV |
| Average HI ionization cross-section $\sigma_N$ | 2.69 x $10^{-22}m^2$ |
| Effective HI ionization cross-section $\sigma_E$ | 2.17 x $10^{-22}m^2$ |
| Speed of light $c$ | 299 792 458 m/s |

**Table 1.** Simulation parameters summary.

of physics at play in haloes and in the IGM. CoDa I and II simulations were extremely heavy because of their very large size. Here, instead, the box size is set to 8 $h^{-1}$Mpc , to keep the computational cost in check, and the initial conditions are generated with mpgrafic (Prunet & Pichon 2013), assuming the Planck cosmology (Planck Collaboration et al. 2014) given in Tab. 1. The possible impact of the smaller box size will be discussed when necessary. We outline below the main physical aspects of the code, highlighting the other differences with CoDa II physics.

To compute the H-ionizing emissivity of stellar particles as a function of their age and metallicity, we use BPASSv2.2.1 stellar population models (Eldridge et al. 2017) with binary stars. This is at variance with CoDa I and II, where emissivity was a step function, whereby a stellar particle would emit for 10 Myr and then be completely dark. We choose the available initial mass function closest to Kroupa (2001) with slopes of -1.3 from 0.1 to 0.5 $M_\odot$ and -2.35 from 0.5 to 100 $M_\odot$. The mass fraction in supernovae is then set to $\eta_{SN} = 0.2$ as in Rosdahl et al. (2018).

Chemical enrichment is accounted for, and allows us to track the increasing metallicity of galaxies gas and stellar content. We use a standard metal yield of $y = 0.1$, in agreement with the BPASS model used, and the starting cosmic metallicity is 0. On average, the ionizing emissivity of a young stellar population decreases with increasing metallicity with this model.

Our stellar particles are relatively massive, close to $10^4$ $M_\odot$, i.e. a star cluster of intermediate mass. Such a cluster does not form its stars instantaneously, but over the course of a few Myr Hollyhead et al. (2015); Wall et al. (2020). To account for this, we model the stellar particle as a population of constant star formation rate over 5 Myr, a timescale compatible with star cluster models of He et al. (2019, 2020) and compute the corresponding time-metallicity-dependent H-ionizing emissivity using the adopted BPASS models. We also compute the effective photon energy, average and effective ionization cross-sections given in Tab. 1, following Rosdahl et al. (2013) Eqs. B3-B5, adopting for this an average absolute metallicity Z=$10^{-3}$ and integrating overs stars up to 10 Myr of age, after which the ionizing emissivity becomes too small to impact the radiative parameters significantly. A change in average metallicity or maximum age of integration affects the resulting photon energy and cross-sections at less than a few percent level, such that it does not affect our results significantly. We use the full speed of light in the radiative transfer module, for the propagation of radiation and its interaction with the Hydrogen gas, so as to avoid possible detrimental artefacts due to the reduced speed of light framework, as reported in Deparis et al. (2019). Of crucial importance for this study, and the Lyman-$\alpha$ forest in general, is the post-overlap residual neutral fraction, which can be strongly impacted by the use of a reduced speed of light, as shown in Ocvirk et al. (2019).

Finally, we will vary the sub-grid star formation model of the 2 main simulations in this paper. One uses a strict threshold temperature for star formation $T_\star = 2.10^4$K, i.e. stars are allowed to form only in cells with lower temperature than $T_\star$, as in CoDa I (Ocvirk et al. 2016). This is a very common, widely used criterion, both in grid-based and Smoothed-Particle-Hydrodynamics codes, e.g. (Stinson et al. 2006; Agertz et al. 2013). The other simulation does not use this criterion, and hence it is closer to the CoDa II setup (Ocvirk et al. 2018). In the latter, star formation is therefore allowed in cells above the threshold density for star formation $\delta_\star$, no matter the temperature. Star formation is therefore more permissive. These 2 simulations will be referred to as "Strict" and "Permissive" in the rest of the paper. There is an underlying physical assumption which subtends these two models. The $T_\star = 2.10^4$K limit is the highest temperature the gas can reach via photo-heating. Therefore, anything hotter is shock-heated, usually by supernovae. Therefore, the Permissive model, by allowing star formation beyond this limit temperature, implicitly assumes that an unspecified fraction of the unresolved cell gas is still in the form of cold gas that could form stars. On the contrary, the Strict model implies that above $T_\star$, the gas is in a shocked state, unable to form stars. For the Strict simulation, because star formation is less permissive than in CoDaII, the star formation efficiency was increased to $\epsilon = 0.03$, and the particle

escape fraction was also increased to 1, while the Permissive run used respectively 0.02 and 0.45 for these parameters. Both simulations ran down to z=4 to allow us to study the post-overlap state of the irradiated IGM.

## 3 RESULTS

### 3.1 Ionized fraction and electron-scattering optical depth

Both simulations are a good match to observational estimates of the cosmic ionized fraction (Greig et al. 2017; Davies et al. 2018; Mason et al. 2018; Hoag et al. 2019), as shown in the left panel of Fig. 1. The evolution of the ionized fraction in both runs is consistent with most of the observed data points. Although the Strict run starts reionizing earlier because of the higher star formation efficiency and particle escape fraction $f_{esc}^{sub}$, it then proceeds slightly slower than the Permissive run, which eventually catches up so that both runs are fully reionized at the same redshift z$\sim$ 6. More precisely, if we define the reionization redshift $z_{rei}$ as the redshift at which the ionized fraction reaches $x_{HII} = 0.99$, the Strict (Permissive) run reionizes at $z_{rei} = 6.039(6.032)$, so that the runs can be considered to effectively reach complete reionization at the same time. The headstart of the Strict run also transpires in the electron scattering optical depth, which is slightly higher than for the Permissive run as shown in the right panel of Fig. 1, although both runs are in good agreement with the observed values of Planck Collaboration et al. (2018).

### 3.2 Lyman-$\alpha$ forest and Gunn-Peterson trough

Although box sizes of $\sim$ 40 $h^{-1}$Mpc and beyond are preferred to study the Lyman-$\alpha$ forest's detailed properties, e.g. PDF, power spectrum, dark gaps and transmission spikes statistics (Bolton & Becker 2009), the *average* effective opacity, while containing less information than the PDF of effective opacities $\tau_{eff}$, is less affected by box size. Indeed, Chardin et al. (2015) shows that the average effective opacity of their 40 $h^{-1}$Mpc box is very similar to that of their 10 $h^{-1}$Mpc box, as shown in their Fig. 12(b). Based on their plot, it seems unlikely that reducing the box size to the 8 $h^{-1}$Mpc setup we use here would suddenly yield a strongly discrepant average $\tau_{eff}$. Moreover, Fig. 10 of Bosman et al. (2018b) shows that although the detailed PDF can be affected by a change of averaging length (from 10 to 50 $h^{-1}$Mpc ), the *average* effective opacity, read as $P(\tau) = 0.5$, remains relatively stable, except around z=6, where the dispersion is the largest. We are therefore confident that our small box size does not strongly bias the *average* effective opacities we compute. However, as a precaution, we will refrain from analyzing $\tau_{eff}$ PDFs obtained from our simulations, as those may be more strongly affected and therefore potentially more difficult to interpret.

We consider 512 random lines of sight (hereafter LoS) of 8/h cMpc length through our volume. Along these LoSs, we compute the Lyman-$\alpha$ opacities of our simulated volume following Chardin et al. (2015, 2017); Chardin et al. (2018), but without any adjustment or renormalization of the flux or neutral fraction values, just using the simulation's raw data. We compute the average opacity of the k-th LoS as:

$$\tau_{eff}^{k} = \log\left(\frac{1}{N}\sum_{i} e^{-\tau_i^k}\right), \quad (1)$$

where log is the Napierian or natural logarithm, $\tau_i^k$ is the opacity of cell i on LoS k, and N is the number of cells spanning the 8 $h^{-1}$Mpc LoS. The average opacity $\tau_{eff}$ of the simulation's IGM is then just the linear average of the 512 $\tau_{eff}^{k}$. The resulting average $\tau_{eff}$ are shown in Fig. 2 as a function of redshift, along with observations from Fan et al. (2006); Becker et al. (2013, 2015); Bosman et al. (2018a). The Permissive run's opacities are significantly lower than observed. The Strict run fares much better in this respect. The agreement is good just after overlap and down to z=5.5, after which the Strict run's average $\tau_{eff}$ sit slightly below the observed cloud of points, before rejoining it around z=4.5. Despite the small offset at $\sim$ 5, the Strict run clearly matches the observations better than the Permissive run, eventhough the reionization redshifts of both runs are equal. Remarkably, the Strict run is more opaque after overlap than the Permissive run, eventhough the Strict run starts reionizing earlier. To understand this, we now turn to further quantities characterizing the gas opacity.

### 3.3 Neutral fraction and ionizing rate

The Lyman=$\alpha$ opacities of the IGM are determined principally by the neutral Hydrogen density on the line of sight considered, which is, in turn, tightly connected to the ionizing rate $\Gamma$. In Fig. 3 we show the hydrogen neutral fraction (left) and the hydrogen ionizing rate in ionized regions (right) for both simulations, and existing observational constraints. The Fan et al. (2006) neutral fractions are shown to guide the eye, but since they are derived from opacities, it is much better to compare direclty the opacities, as we did in Fig. 2. Although reionization happens in both runs at precisely the same redshift, the neutral fractions of the Permissive run are smaller than the Strict run's by a factor $\sim$ 5 at z=4, which explains their difference in opacity.

The origin of this difference in post-overlap neutral fraction can be traced back to differences in ionizing rates, as seen in the right panel of Fig. 3. The evolution of the ionizing rate exhibits a sharp surge at overlap (close to z=6), and a slow saturation afterwards, as seen in most of the literature Aubert & Teyssier (2010); Ocvirk et al. (2016); Rosdahl et al. (2018); Ocvirk et al. (2018). While, the Strict run is in good agreements with the observations of Faucher-Giguère et al. (2008); Calverley et al. (2011); Becker & Bolton (2013); D'Aloisio et al. (2018), the Permissive run overshoots them by a factor $\sim$ 5, which explains the difference in neutral fractions.

In order to understand how this difference in ionizing rate arises, we turn to studying the collective escape emissivity of the star-forming haloes of our simulations.

### 3.4 Galaxy populations and their ionizing photon output

Here we use the formalism of Lewis et al. (2020), who computed the photon budget of galaxies in the Cosmic Dawn II simulation (Ocvirk et al. 2018) to compare the behaviour of the Strict and Permissive runs in terms of halo ionizing emissivities. In all of this discussion of our results, we discuss only the dark matter halo mass of haloes and may therefore use the term mass without further distinction, since stellar mass will not be considered.

We use RAMSES's on-the-fly clump finder PHEW (Bleuler et al. 2015) to detect dark matter haloes with the parameters indicated in the paper. Then we use $R_{200}$ as a proxy to the virial radius, and compute each halo's ionizing escape fraction at $R_{200}$ via ray-tracing as in Lewis et al. (2020). The halo ionizing escape emissivity is then the product of the intrinsical ionizing emissivity of its stellar population, taken from the BPASS model we used, and its halo escape fraction. We then compute the total escape emissivity

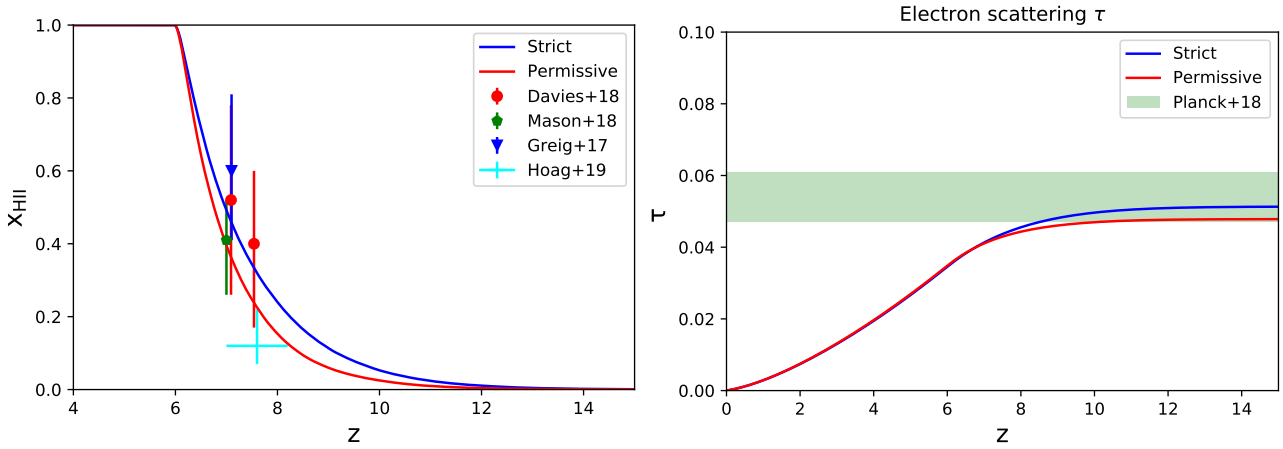


Figure 1: Cosmic ionized fraction (left) and electron-scattering optical depth (right) from the simulations and comparison with observations.

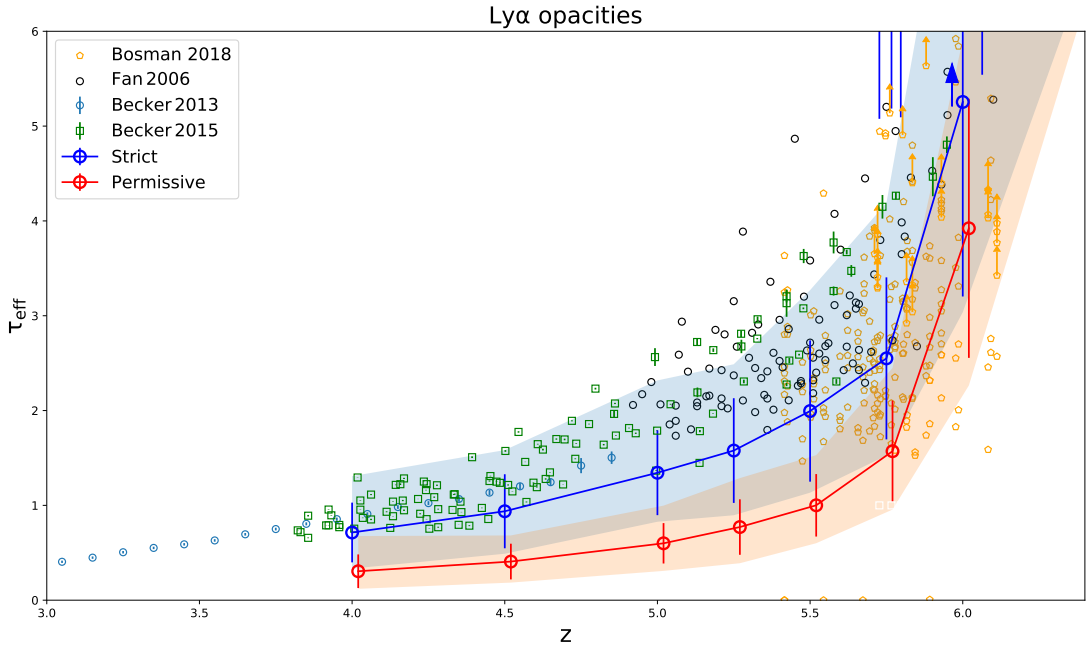


Figure 2: Lyman-$\alpha$ effective optical depths predicted by our runs, and from observations. The solid blue (red) line shows the average of the effective optical depths of the Strict (Permissive) run, and their standard deviation as a vertical bar. The blue (orange) shaded area shows the extent of the 5-95 percentile of the distribution. The Permissive and Strict data have been shifted by 0.02 in redshift, to improve lisibility.

$\dot{n}_{esc}$ of the full halo population as the sum of the escape emissivities of all the haloes in the simulation divided by the comoving volume of the box. For a number of reasons, ranging from imperfect halo detection at the low mass end to over-linking, some stars may lack an associated halo, as was already noted in Ocvirk et al. (2018). As a consequence, these stars are not accounted for in individual halo emissivities. To account for them in our analysis, we correct the total escape emissivity $L_{tot}$ using a correction factor defined as

$$f_{cor} = SFR_{fullbox}/SFR_{haloes}\,, \quad (2)$$

where $SFR_{fullbox}$ is the SFR of the full computational volume, and $SFR_{haloes}$ is the total SFR taking place in haloes. This correction factor varies from about 1.5 at z=10 to 1.1 at z=4.

With this correction implemented, we show the total escape emissivity $\dot{n}_{esc}$, for our 2 simulations in Fig. 4, as solid lines. The difference in evolution is striking: the Permissive run rises monotonously, and starts to level at z=5.5, whereas the Strict run's total emissivity increases up to z=6 and then *decreases* onwards. This difference in halo emissivity explains the different evolutions of the ionizing rates in the two simulations. We recall here that AGNs are not accounted for in our simulations, and that they may contribute significantly by the end of our runs, at z=4, as seen in Dayal et al. (2020). We plan to explore this aspect once we have upgraded our code to model AGNs, in a future paper.

The overall evolution of the emissivity of the Strict run is rem-

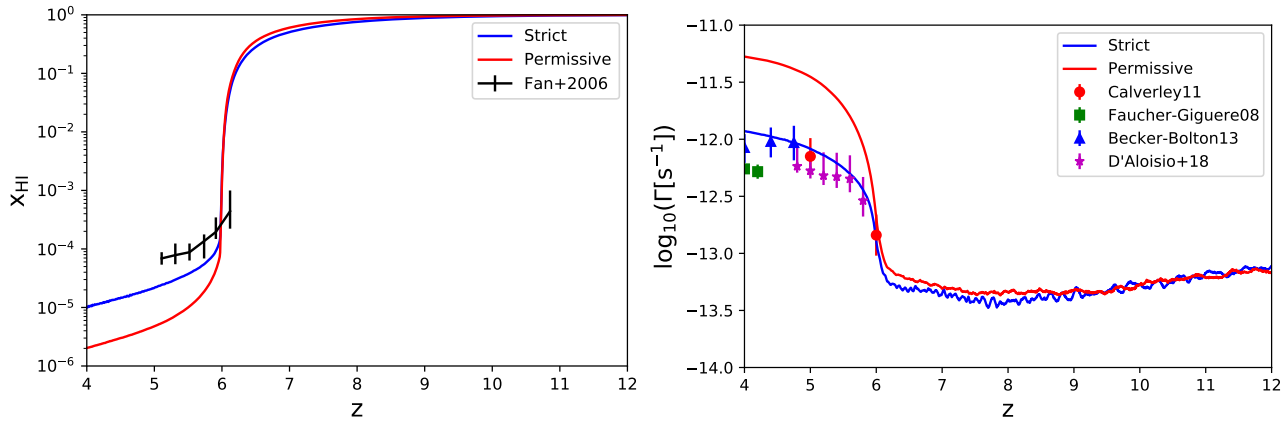


Figure 3: Cosmic neutral Hydrogen fraction (left) and Hydrogen ionizing rate in ionized regions (right) from the simulations and comparison with observations.

iniscent of that reported by K19, who found that a non-monotonic, rising then falling, emissivity, was required to reproduce the Lyman-$\alpha$ opacities at the end of the EoR. It may come as a surprise that, although the emissivity of our Strict run is lower than that of K19, it reionizes earlier. We caution however that our emissivities are perhaps not directly quantitatively comparable to theirs. Indeed, their spatial resolution is of $\sim 80\ h^{-1}$Mpc comoving (about 8 times coarser than used here). At this resolution, massive haloes may still span a few grid cells in virial radius, and absorption of ionizing photons between the halo center and the virial radius, i.e. through the circum-galactic medium (hereafter CGM), mostly, happens, and is resolved by their radiative transfer prodedure. Therefore all of their emissivity does not necessarily reach the IGM. In contrast, thanks to the determination of our halos' escape fractions, our emissivity is a measure of what comes out of the halo population at the virial radius, and therefore directly into the IGM. Because of this difference, it is expected that K19 would require a higher emissivity than our runs to obtain a comparable reionization history for the same box size. On top of this, their box size is larger, and larger boxes take longer to reionize at fixed emissivity. Considering these 2 aspects, their lower reionization redshift despite higher overall emissivity is not an issue. Therefore, we can not expect the agreement with K19 to be fully quantitative, but the qualitative agreement in the shape of the evolution of the emissivity, namely its rise and fall, is our main result here.

We now proceed to gain better insight into our results. In order to understand why the emissivities of the two runs are so different, we divided the total emissivity in a low mass and a high mass halo contribution, with a threshold at $2.10^9 M_\odot$. We use this threshold because it was determined to separate haloes sensitive to radiative feedback and haloes immune (in a star-foming sense) to the rise of the ionizing radiation field in our framework, as found in (Ocvirk et al. 2016; Dawoodbhoy et al. 2018; Ocvirk et al. 2018), and in agreement with e.g. Pawlik et al. (2015); Wu et al. (2019a). With this distinction, we see from Fig. 5 that indeed the contribution of low mass haloes decreases after reionization at z=6. The decrease occurs earlier for the Strict run than the Permissive run. Before z=6, though, the low mass haloes' contribution to the total emissivity is the main driver of cosmic reionization, as it is larger than that of the high mass haloes. The latter take over when the low mass population peters out. Eventhough they start to contribute later, because the massive halo population first needs to build up, once they are on the rise, their contribution increases monotonously. In the Strict run, the post-overlap decreasing total emissivity is the result of the demise of the low mass halo population, which the rise of the high mass counterpart does not compensate.

While the details of the mechanisms involved in decreasing the emissivity in K19 are not explicitly given, our result sheds new light onto the origin of this peculiar evolution: it arises from the combination of a gradually suppressed population of low mass haloes driving reionization up to shortly before the overlap, when the contribution of high mass haloes starts to become significant. However, the latter contribution does not rise fast enough to compensate the quickly dimming low mass haloes, and the resulting total emissivity therefore decreases.

The later, and slightly shallower decrease in emissivity of the low mass haloes seen in the Permissive run compared to the Strict run is expected, as it originates from a difference in SFR suppression. Such a difference was already reported in Ocvirk et al. (2018). It is further supported and confirmed by Fig. 6, which shows the SFR of haloes in the low mass range ($2.5 < M/10^8 M_\odot < 7.5$) as a function of time (the masses quoted are instantaneous): the low mass haloes in the Strict run see their SFR suppressed more strongly than in the Permissive run. In contrast, $5.10^9 M_\odot$ haloes, belonging to the high mass group, see their SFR unaffected by the occurence of reionization. The shallow decrease they experience, in both runs, is of purely cosmological origin, and a similar behaviour was reported in cosmological simulations of galaxy formation without radiative transfer (Ocvirk et al. 2008). In summary, Fig. 6 confirms the suppression of SFR as the origin of the decrease of the low mass halo emissivity.

We note that the high mass haloes display significantly higher emissivities in the Permissive versus Strict runs. This is not expected from their SFR, which is fairly similar in both runs, as can be appreciated from the $5.10^9 M_\odot$ track of Fig. 6. If the high mass haloes' SFRs are similar in the Strict and Permissive runs, then to allow the Permissive run's emissivity to be larger than the Strict run's, their escape fraction must be different. This is indeed the case, as shown by Fig. 7, which represents the average ray-tracing escape fraction of all haloes, averaged over all redshifts, as a function of mass, for each run. Both saturate close to unity for low masses, but the escape fractions of the Strict run start dropping at lower masses than the Permissive run's and they drop more steeply. This difference is due to the Permissive run allowing stars to form in cells with temperatures potentially higher than $2.10^4$ K, i.e. intrinsically more ionized and therefore transparent than the Strict run's.

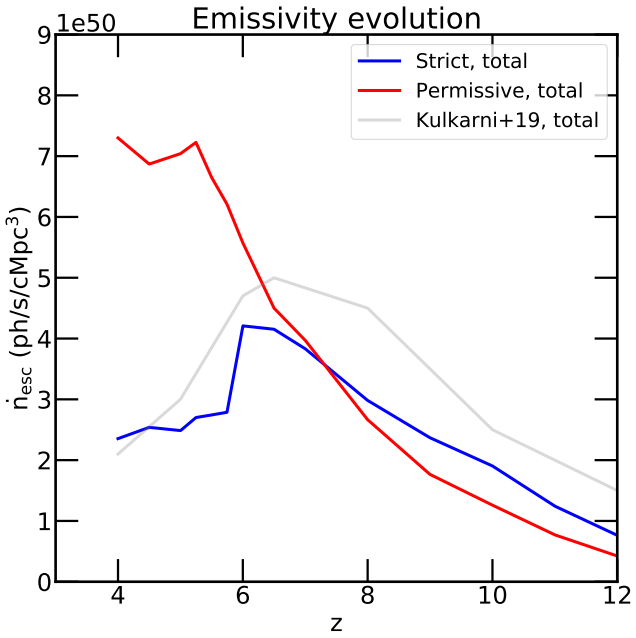


Figure 4: Total Emissivities of our 2 simulations. The blue (red) solid line shows the total emissivity of the Strict (Permissive) run. The gray solid line shows the results of K19 for comparison.

Note, however, that in order for the Permissive run to complete reionization by z$\sim$ 6, like the Strict run, we had to use a stellar particle escape fraction $f_{esc}^{sub} = 0.45$. Therefore, following the definitions in Lewis et al. (2020), the net escape fraction for the Permissive run's is the ray-tracing escape fraction times $f_{esc}^{sub} = 0.45$, as shown by the dotted line in Fig. 7.

As a caveat, we note that the box size used here may not be sufficient to sample well the high mass end of the galaxy population. This is may not be very important for the Strict run, because the high mass escape fractions are fairly low. However, for the Permissive run, escape fractions of high mass haloes are significantly larger, which makes them more important in the galactic photon budget, and therefore we may be missing their contribution or a fraction thereof because of the limited box size. For this reason, we refrain here from comparing directly our photon budget with Lewis et al. (2020) and defer this comparison and deeper investigation to a later paper using Cosmic Dawn III, which will be 512 times larger, when it will be fully available for analysis.

## 4 CONCLUSIONS

We have presented radiation-hydrodynamical simulations of the EoR with RAMSES-CUDATON, using two different sub-grid star formation models, tuned to reionize both at z=6, and analyzed their resulting Lyman-$\alpha$ opacities. The latter were then interpreted by looking at the emissivity of galaxy populations in both simulations. We find that the simulation best matching the observed quasar line-of-sight Lyman-alpha opacities is the Strict run, where star formation is allowed only below a gas temperature threshold of $T_\star = 2.10^4$K, which promotes stronger radiative suppression, and escape fractions steeply declining with halo mass. In this run, reionization is driven by a low mass halo population, up to overlap. At z=6, this population is radiatively suppressed due to the rising ionizing UV background, and its emissivity drops. In the meantime, the high mass halo population builds up and its emissivity rises, but not fast enough to compensate the dimming low mass one. The combined emissivity of these two populations therefore features a rise and fall, from z=12 to z=4, with a peak at z$\sim$ 6. In contrast, our other run, with more permissive star formation, displays a more continued increase in emissivity, and as a result overshoots the observed ionizing rate and produces an overly transparent Universe after z=6, as shown by its low Lyman-$\alpha$ opacity. This suggests that a z=6 - peaked rather than continuously rising emissivity is required to avoid over-ionizing the Lyman-alpha forest after overlap. External radiative suppression of star formation in low mass haloes is a crucial mechanism in modulating the transmission properties of the Lyman-alpha forest during the EoR and after overlap. The difference between the emissivities of the two runs occurs in two ways: the Strict run features stronger and earlier suppression at reionization, but also yields more steeply decreasing escape fractions with increasing halo mass, preventing the high mass halo population from compensating the low mass's dropping emissivity.This highlights the impact of the star formation sub-grid model not only on the SFR and its sensitivity to radiation, but also on the halo escape fraction.

While the Strict run's Lyman-alpha optical depths fare better than the Permissive run's, there is still room for improvement. We foresee several directions to test and try for an improved agreement with observations. It is possible that aiming for a lower reionization redshift could help, as in K19 and Keating et al. (2019), however that may come at the cost of undershooting the Planck electron-scattering optical depth. In this direction, it is likely that using a larger volume would help us improve the significance of our study with respect to both observables. This aspect will be addressed with the upcoming Cosmic Dawn III simulation, which will be 512 times larger in volume, at the same spatial and mass resolution, and will therefore be a unique asset to extend current results.

We also plan to improve the physics of the simulation by modelling dust formation, and investigate the impact of this potentially important process on the evolution of the emissivity of the galaxies in our simulations. This will allow us to check which effect, radiative suppression of the high escape fraction population, or dust formation, as invoked in Puchwein et al. (2019), contributes the most to the decrease of the cosmic emissivity.

## ACKNOWLEDGEMENTS

This study was performed in the context of several French ANR (Agence Nationale de la Recherche) projects. PO acknowledges support from the French ANR funded project ORAGE (ANR-14-CE33-0016). The simulations in this study were performed on Jean Zay at Institut du Developpement et des Ressources en Informatique Scientifique (IDRIS) through several DARI and Grand Challenge allocations. The authors would like to acknowledge the High Performance Computing center of the University of Strasbourg for supporting this work by providing scientific support and access to computing resources. This work made use of v2.2.1 of the Binary Population and Spectral Synthesis (BPASS) models as last described in Eldridge et al. (2017).

## References

Agertz O., Kravtsov A. V., Leitner S. N., Gnedin N. Y., 2013, ApJ, 770, 25
Aubert D., Teyssier R., 2008, Monthly Notices of the Royal Astronomical Society, 387, 295
Aubert D., Teyssier R., 2010, The Astrophysical Journal, 724, 244

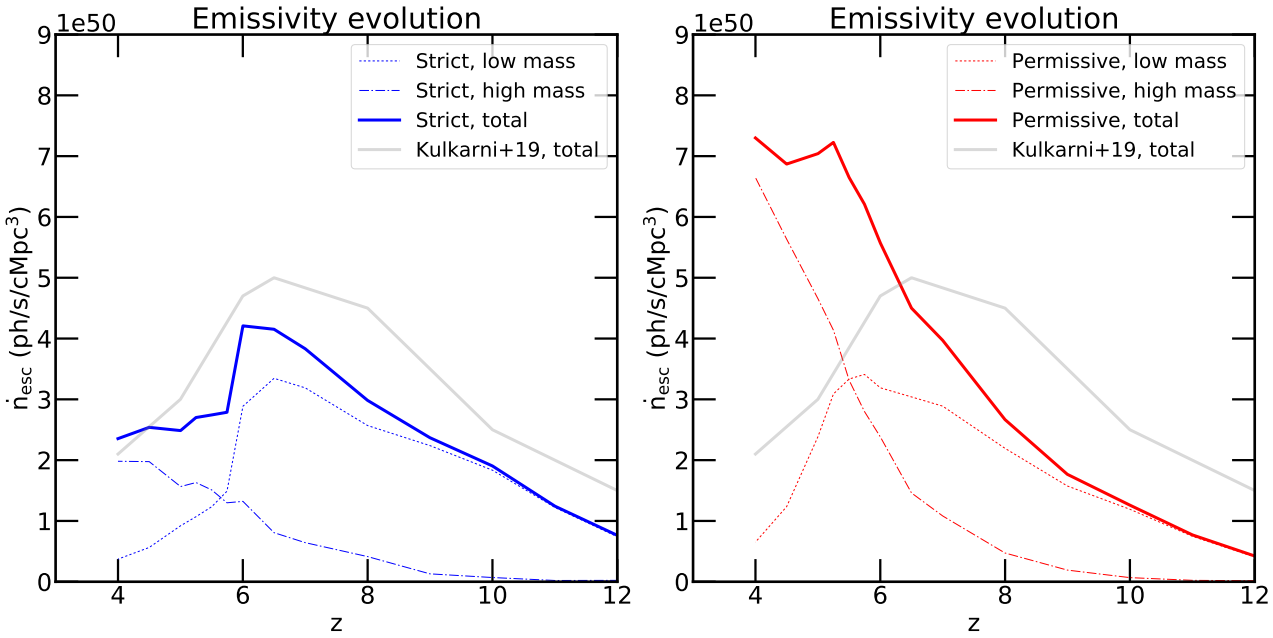


Figure 5: Emissivities of our 2 simulations, detailed in two mass bins. The threshold between high and low mass haloes is set at $2.10^9 M_\odot$. The blue (red) solid line shows the emissivity of the Strict (Permissive) run. The gray solid line shows the results of K19 for comparison.

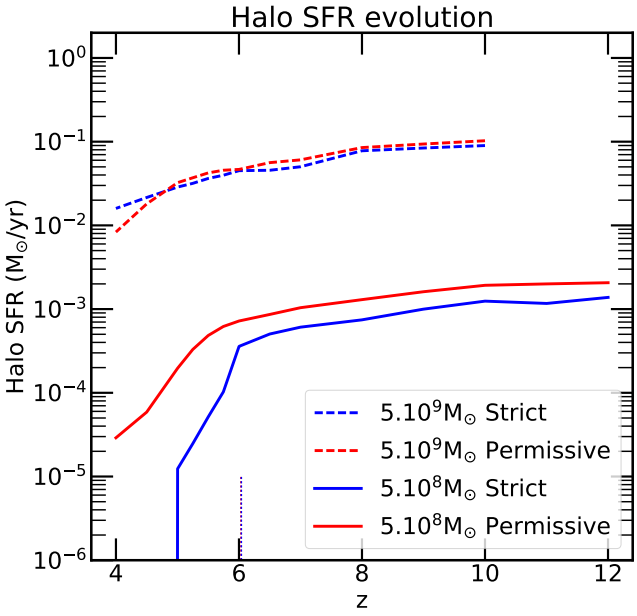


Figure 6: Star formation rate of dark matter haloes in the range $2.5 - 7.5 \times 10^8 M_\odot$, i.e. centered on $5.10^8 M_\odot$, for the Strict (blue, solid) and Permissive (red, solid) runs. The dashed lines show the SFRs of the $2.5 - 7.5 \times 10^9 M_\odot$ bin, i.e. centered on $5.10^9 M_\odot$ bin. The short vertical dotted lines, blue and red, practically on top of each other, show the reionization redshift of both simulations.

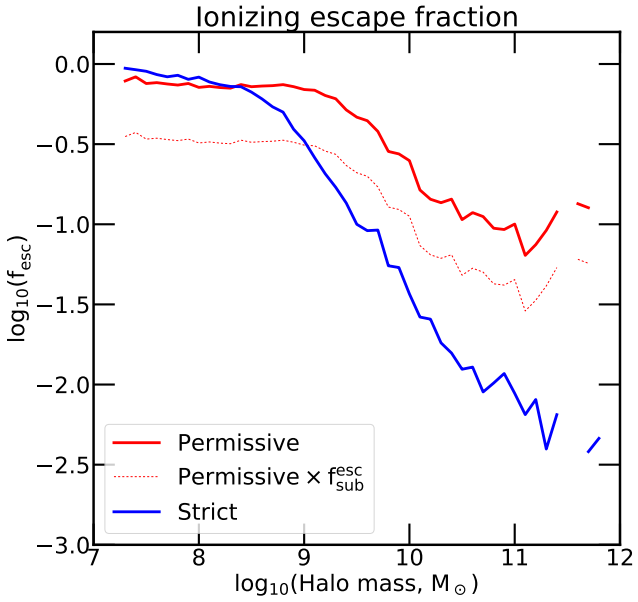


Figure 7: Ray-tracing halo escape fractions measured in our 2 simulations. The lines show the averages of all haloes at all redshifts, for the mass bins considered. For the Permissive run, the dotted line shows the net halo escape fraction, i.e. the ray-tracing escape fraction multiplied by the stellar particle escape fraction, or sub-grid escape fraction, $f_{esc}^{sub} = 0.45$. For the Strict run, the net halo escape fraction is equal to the ray-tracing escape fraction, since $f_{esc}^{sub} = 1$.

Aubert D., Deparis N., Ocvirk P., 2015, Monthly Notices of the Royal Astronomical Society, 454, 1012
Aubert D., et al., 2018, The Astrophysical Journal Letters, 856, L22
Bauer A., Springel V., Vogelsberger M., Genel S., Torrey P., Sijacki D., Nelson D., Hernquist L., 2015, MNRAS, 453, 3593
Becker G. D., Bolton J. S., 2013, MNRAS, 436, 1023
Becker G. D., Hewett P. C., Worseck G., Prochaska J. X., 2013, MNRAS, 430, 2067
Becker G. D., Bolton J. S., Madau P., Pettini M., Ryan-Weber E. V., Venemans B. P., 2015, MNRAS, 447, 3402
Bleuler A., Teyssier R., Carassou S., Martizzi D., 2015, Computational Astrophysics and Cosmology, 2, 5
Bolton J. S., Becker G. D., 2009, MNRAS, 398, L26
Bosman S. E. I., Fan X., Jiang L., Reed S. L., Matsuoka Y., Becker G. D.,

Haehnelt M. G., 2018a, arXiv:1802.08177 [astro-ph]
Bosman S. E. I., Fan X., Jiang L., Reed S., Matsuoka Y., Becker G., Haehnelt M., 2018b, MNRAS, 479, 1055
Bouwens R. J., Illingworth G. D., Oesch P. A., Caruana J., Holwerda B., Smit R., Wilkins S., 2015, The Astrophysical Journal, 811, 140
Calverley A. P., Becker G. D., Haehnelt M. G., Bolton J. S., 2011, Monthly Notices of the Royal Astronomical Society, 412, 2543
Chardin J., Haehnelt M. G., Aubert D., Puchwein E., 2015, Monthly Notices of the Royal Astronomical Society, 453, 2943
Chardin J., Puchwein E., Haehnelt M. G., 2017, Monthly Notices of the Royal Astronomical Society, 465, 3429
Chardin J., Kulkarni G., Haehnelt M. G., 2018, MNRAS, 478, 1065
D'Aloisio A., McQuinn M., Davies F. B., Furlanetto S. R., 2018, MNRAS, 473, 560
Davies F. B., et al., 2018, ApJ, 864, 142
Dawoodbhoy T., et al., 2018, Monthly Notices of the Royal Astronomical Society, 480, 1740
Dayal P., et al., 2020, arXiv, p. arXiv:2001.06021
Deparis N., Aubert D., Ocvirk P., Chardin J., Lewis J., 2019, Astronomy and Astrophysics, 622, A142
Eldridge J. J., Stanway E. R., Xiao L., McClelland L. A. S., Taylor G., Ng M., Greis S. M. L., Bray J. C., 2017, Publications of the Astronomical Society of Australia, 34, e058
Fan X., et al., 2006, The Astronomical Journal, 132, 117
Faucher-Giguère C.-A., Lidz A., Hernquist L., Zaldarriaga M., 2008, ApJ, 682, L9
Gnedin N. Y., 2016, The Astrophysical Journal, 833, 66
Gnedin N. Y., Kaurov A. A., 2014, ApJ, 793, 30
Greig B., Mesinger A., Haiman Z., Simcoe R. A., 2017, MNRAS, 466, 4239
He C.-C., Ricotti M., Geen S., 2019, MNRAS, 489, 1880
He C.-C., Ricotti M., Geen S., 2020, MNRAS, 492, 4858
Hoag A., et al., 2019, ApJ, 878, 12
Hollyhead K., Bastian N., Adamo A., Silva-Villa E., Dale J., Ryon J. E., Gazak Z., 2015, MNRAS, 449, 1106
Katz H., Kimm T., Haehnelt M., Sijacki D., Rosdahl J., Blaizot J., 2018, arXiv:1802.01586 [astro-ph]
Katz H., Kimm T., Haehnelt M. G., Sijacki D., Rosdahl J., Blaizot J., 2019, Monthly Notices of the Royal Astronomical Society, 483, 1029
Keating L. C., Weinberger L. H., Kulkarni G., Haehnelt M. G., Chardin J., Aubert D., 2019, arXiv e-prints, p. arXiv:1905.12640
Kroupa P., 2001, Monthly Notices of the Royal Astronomical Society, 322, 231
Kulkarni G., Keating L. C., Haehnelt M. G., Bosman S. E. I., Puchwein E., Chardin J., Aubert D., 2019a, Monthly Notices of the Royal Astronomical Society: Letters, 485, L24
Kulkarni G., Worseck G., Hennawi J. F., 2019b, MNRAS, 488, 1035
Lewis J. S. W., et al., 2020, arXiv e-prints, 2001, arXiv:2001.07785
Madau P., 2017, ApJ, 851, 50
Mason C. A., Treu T., Dijkstra M., Mesinger A., Trenti M., Pentericci L., de Barros S., Vanzella E., 2018, The Astrophysical Journal, 856, 2
Matsuoka Y., et al., 2018, ApJ, 869, 150
Mitra S., Choudhury T. R., Ferrara A., 2018, MNRAS, 473, 1416
Naidu R. P., Tacchella S., Mason C. A., Bose S., Oesch P. A., Conroy C., 2020, ApJ, 892, 109
Ocvirk P., Pichon C., Teyssier R., 2008, Monthly Notices of the Royal Astronomical Society, 390, 1326
Ocvirk P., et al., 2016, Monthly Notices of the Royal Astronomical Society, 463, 1462
Ocvirk P., et al., 2018, eprint arXiv:1811.11192
Ocvirk P., Aubert D., Chardin J., Deparis N., Lewis J., 2019, Astronomy and Astrophysics, 626, A77
Pawlik A. H., Schaye J., Dalla Vecchia C., 2015, Monthly Notices of the Royal Astronomical Society, 451, 1586
Petkova M., Springel V., 2011, MNRAS, 412, 935
Planck Collaboration et al., 2014, A&A, 571, A16
Planck Collaboration Aghanim N., Akrami Y., Ashdown M., Aumont J., Baccigalupi C., Ballardini 2018, arXiv e-prints, p. arXiv:1807.06209
Prunet S., Pichon C., 2013, Astrophysics Source Code Library, p. ascl:1304.014
Puchwein E., Haardt F., Haehnelt M. G., Madau P., 2019, Monthly Notices of the Royal Astronomical Society
Rosdahl J., Blaizot J., Aubert D., Stranex T., Teyssier R., 2013, Monthly Notices of the Royal Astronomical Society, 436, 2188
Rosdahl J., et al., 2018, Monthly Notices of the Royal Astronomical Society
So G. C., Norman M. L., Reynolds D. R., Wise J. H., 2014, ApJ, 789, 149
Stinson G., Seth A., Katz N., Wadsley J., Governato F., Quinn T., 2006, MNRAS, 373, 1074
Teyssier R., 2002, Astronomy & Astrophysics, 385, 337
Wall J. E., Mac Low M.-M., McMillan S. L. W., Klessen R. S., Portegies Zwart S., Pellegrino A., 2020, ApJ, 904, 192
Wise J. H., 2019, arXiv e-prints, p. arXiv:1907.06653
Wu X., Kannan R., Marinacci F., Vogelsberger M., Hernquist L., 2019a, Monthly Notices of the Royal Astronomical Society, p. 1681
Wu X., McQuinn M., Kannan R., D'Aloisio A., Bird S., Marinacci F., Davé R., Hernquist L., 2019b, arXiv e-prints, p. arXiv:1907.04860
Yoo T., Kimm T., Rosdahl J., 2020, arXiv e-prints, 2001, arXiv:2001.05508
Zawada K., Semelin B., Vonlanthen P., Baek S., Revaz Y., 2014, MNRAS, 439, 1615

This paper has been typeset from a TEX/LATEX file prepared by the author.